Available online at www.sciencedirect.com
ScienceDirect
Trans. Nonferrous Met. Soc. China 33(2023) 1827−1838
Transactions of Nonferrous Metals Society of China
www.tnmsc.cn

Corrosion characteristics of Sn−20Bi−*x*Cu−*y*In solder in 3.5% NaCl solution

Da QI[1,2,3], Wen-chao YANG[1,2,3], Shi-wei JIANG[1,2,3], Yao-kun FU[1,2,3], Qian-qian SONG[1,2,3], Yong-zhong ZHAN[1,2,3]

1. School of Resources, Environment and Materials, Guangxi University, Nanning 530004, China;
2. State Key Laboratory of Featured Metal Materials and Life-cycle Safety for Composite Structures, Nanning 530004, China;
3. MOE Key Laboratory of New Processing Technology for Nonferrous Metals and Materials, Nanning 530004, China

Received 9 January 2022; accepted 16 August 2022

Abstract: The corrosion behaviors of Sn−20Bi−*x*Cu−*y*In (*x*=0.3, 0.5 wt.%; *y*=1, 2, 3 wt.%) in 3.5 wt.% NaCl solution at room temperature were investigated. Electrochemical impedance spectroscopy (EIS) plots, potentiodynamic polarization curves, and corroded surface product characterization were used to evaluate the corrosion resistance of the solders. Analysis of EIS and polarization curves shows that the corrosion resistance of the solders decreases as the In and Cu contents increase. Scanning electron microscopy, energy dispersive spectroscopy, X-ray diffraction, and X-ray photoelectron spectroscopy were applied to characterizing the corrosion product. It is found that the corrosion product is $Sn_3O(OH)_2Cl_2$, which cannot play a protective role because of its loose structure. Sn−20Bi−0.3Cu−1In has the best corrosion resistance.

Key words: lead-free solder; corrosion behavior; electrochemical impedance spectroscopy; polarization curve; $Sn_3O(OH)_2Cl_2$

1 Introduction

In the past, Sn−Pb alloy was widely used in the manufacturing industry to provide good mechanical properties at a lower cost [1]. The toxicity of lead poses a significant hazard to humans and the environment. Lead-free solder alloys are essential for the “green manufacturing” and “environmentally friendly” aspects of the electronics industry [2]. Corrosion resistance is a critical factor in the long-term adoption of solders [3].

At present, solders are mainly binary and ternary alloys containing Sn. Binary alloy systems include Sn−Ag, Sn−Zn, Sn−Bi, and ternary alloys include Sn−Bi−Sb, Sn−Zn−In, and others. Sn−Zn alloys have poor corrosion and oxidation resistance, which limits the application of this system [4]. Due to the solid solution formed by the mixing of Sb and Sn, Sn−Sb alloy has low corrosion resistance [5]. As the most promising alternative to Sn−Pb alloys, Sn−*x*Ag−Cu has lower melting temperature, lower coefficient of thermal expansion, better mechanical properties, and higher wettability [6]. Due to the high cost of the Sn−Ag−Cu alloy, much research is being done on alloys with less silver [7].

The Sn−Bi system is an up-and-coming alternative. Sn−Bi solder has better wetting properties and higher tensile strength, and Bi is abundant, so it is more promising for use in low-temperature brazing materials [8]. Compared with the Sn−Pb system, Sn−Bi eutectic solder has lower melting temperature, better tensile strength, and better creep resistance [9]. The eutectic temperature of the Sn−58Bi alloy is 138 °C, and the alloy is formulated in the melting temperature range of 138−232 °C [10]. A large amount of Bi is solutionized in the Sn matrix, and no compound is formed. When the content of Bi in the alloy is 20 wt.%, the melting temperature range is 138−211 °C, and the melting point is close to that of the

Corresponding author: Wen-chao YANG, E-mail: ywch053@163.com
DOI: 10.1016/S1003-6326(23)66225-9

Sn−37Pb eutectic solder. Compared with the Sn−58Bi alloy, Sn−20Bi reduces the Bi content with high resistivity, significantly improving the solder's electrical and thermal conductivity. While maintaining wettability, the adverse effects of Bi can be decreased by reducing the content of Bi in Sn−Bi solder [10]. With the addition of Cu to the Sn−Bi alloy, fine Cu_6Sn_5 intermetallic compounds are formed to improve the bonding performance and reliability of the solder joint. The addition of Cu can significantly improve the coarsening of the Bi-rich phase in the tissue. The addition of In enhances the tensile strength of the alloy while reducing the melting temperature of the alloy. The corrosion behavior of the solder is equally vital without sacrificing excellent mechanical and microstructural properties. ROSALBINO et al [11] investigated the corrosion behavior of Sn−Ag alloys with the addition of In, Bi, and Cu. They found that the 96.1Sn−3.1Ag−0.8Cu alloy was the best in terms of corrosion resistance. LI et al [12] showed that lead-free solders have lower passivation current density values and more expansive passivation areas than Sn−Pb solders.

With the development of marine resources, an increasing number of electronic devices will operate in the marine atmosphere for a long time. Marine atmospheric chemical reactions on metal surfaces result in corrosion products that can short-circuit electronic equipment [13,14]. Therefore, it is necessary to study the initial corrosion evolution of Sn−Bi solders in the marine atmosphere.

The corrosion resistance should be fully considered early in material development to ensure reliability. To date, research on the addition of Cu and In to Sn−20Bi based solder alloys has focused on the effect of the solder microstructure. Studies on corrosion evolution and corrosion product formation mechanisms have rarely been reported. In this study, a 3.5 wt.% NaCl solution was used to simulate the marine atmosphere, and potentiodynamic polarization tests were used to study the corrosion behavior of Sn−20Bi−*x*Cu−*y*In solders. The expected findings are essential for understanding the long-term corrosion behavior of Sn−20Bi−*x*Cu−*y*In solders and their potentials in guiding the maintenance of electronic devices for the safe operation and stability in the marine atmospheric environment.

2 Experimental

2.1 Preparation of electrochemical corrosion samples

In this experiment, Sn−20Bi−*x*Cu−*y*In was prepared by melting using commercially pure Sn (99.99%), pure Bi (99.99%), pure In (99.99%), and pure Cu (99.99%). A molten salt with LiCl/KCl mass ratio of 1:1.3 was prepared. The temperature of the muffle furnace was kept at 600 °C. When the molten salt was melted, the measured Sn, Bi, In, and Cu were added and stirred thoroughly. The samples were poured into the mold to prepare Sn−20Bi−*x*Cu−*y*In (*x*=0.3, 0.5 wt.%; *y*=1, 2, 3 wt.%). The test surface of the alloy sample was ground with 400, 1000, 2000, 3000, and 5000 grit sandpaper, respectively.

2.2 Electrochemical tests

The surface area exposed to the test solution was 0.785 mm^2, and all the experiments were performed at room temperature ((25±0.1) °C). The corrosion medium was 3.5 wt.% NaCl solution. Before the test, samples were immersed in test solutions for 1 h to make the samples reach a stable state. Every test was performed at least 3 times to guarantee satisfactory reproducibility. The experiments were carried out on a CHI660 electrochemical workstation manufactured by Shanghai CH Instrument. This workstation adopted the traditional three-electrode configuration. The reference electrode was a saturated calomel electrode (SCE) and a platinum (Pt) electrode was a counter electrode, as shown in Fig. 1. After waiting for 900 s to ensure that all the experiments were the same, EIS measurements were started. Because the EIS test was performed at open-circuit potential, and unsteady-state conditions may distort the measurement, 900 s was considered sufficient to stabilize the potential. The potential amplitude was set to be 10 mV (vs SCE) at peak-to-peak (AV signal) in an open-circuit, with 5 points per decade, and the frequency range was set from 0.01 to 100000 Hz. The measurement voltage range is from −2 to 2 V.

A low scanning rate can reduce the distortion of the polarization curve. When the scanning rate is low, the interference of the charging current can be ignored, so the distortion of the polarization

curve of the potentiodynamic potential can be ignored [15]. To reduce the distortion of the polarization curve of the potentiodynamic potential, the scanning rate was 0.002 V/s, ranging from −2.5 to 0.5 V. The corrosion current density (J_{corr}) and AC impedance were calculated and fitted by the electrochemical fitting CVIEW2 software, where the polarization curve is a more intuitive way to reflect the corrosion performance of the material.

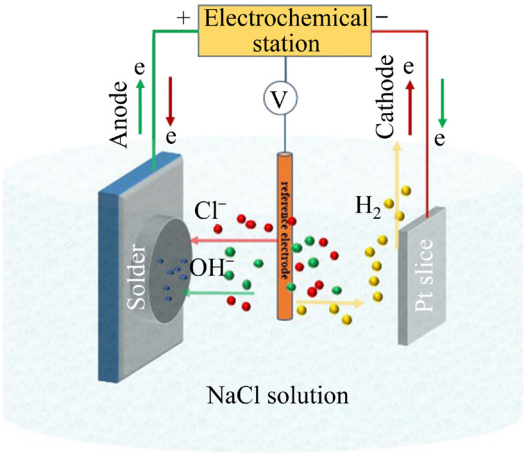

Fig. 1 Schematic diagram of Sn−20Bi−*x*Cu−*y*In (*x*=0.3, 0.5 wt.%; *y*=1, 2, 3 wt.%) alloy electrode polarization measurement devices

Scanning electron microscopy (SEM) with energy dispersive spectroscopy (EDS) was used to observe the corrosion morphology of the sample surface and the composition of surface corrosion products after the polarization test. X-ray photo-electron spectroscopy (XPS) was used to examine the composition and valence states of the elements in the products of electrochemical corrosion.

3 Results and discussion

3.1 Equivalent circuit

Figure 2 shows the equivalent circuit diagrams that fit the experimentally obtained EIS data, where R_s represents the solution resistance; CPE_{dl} represents the capacitance caused by the double-electric layer at the interface between the electrode and the electrolyte (capacitive impedance of the corrosion product layer); R_{ct} represents the charge transfer resistance of the corrosion reaction (corrosion product resistance); CPE_1 represents the capacitive impedance at the interface between the corrosion product layer and the solder substrate bilayer; R_1 represents the resistance at the interface between the corrosion product and the solder substrate bilayer. The Nyquist and Bode plots are shown in Fig. 3. It is not a standard semi-circle, which may be due to various factors such as surface roughness, frequency dispersion of time constants, porous transport effects, and dispersion effects [16]. The high-frequency impedance spectrum is related to the properties of Sn−20Bi−*x*Cu−*y*In. The low-frequency impedance spectrum is related to the charge transfer process between the corrosion product layer and the solder substrate. This factor is related to the two equivalent circuit parts made up of resistors and capacitors connected in parallel.

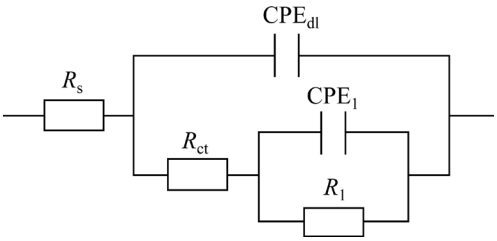

Fig. 2 Equivalent circuit used for fitting experimental EIS data

3.2 EIS results

Figure 3(a) shows that each Nyquist plot is composed of two capacitive semi-arcs, indicating that the solder system is equivalent to two resistor-capacitive circuits [17]. All samples consist of semicircular loops from high to low frequencies. The Nyquist data in the low frequency range indicate the hybrid electrochemical−concentration polarization. The low frequency range of the Nyquist data is determined by the activation energy of the electrochemical reaction, the ionic diffusion rate in the corrosion product layer, and the solder base layer. It is considered that the surface corrosion product layer affects the transmission of ions through this layer [18,19]. It is suggested that the electrode process is controlled by electro-chemical steps. The Nyquist plots show a decrease in the capacitive semi-arcs, where a decrease in the semi-arcs indicates a decrease in corrosion resistance [20]. Figure 3(a) shows that the Sn−20Bi−0.3Cu−3In sample has the smallest capacitive arc radius, which means that it has the worst corrosion resistance. In contrast, the Sn−20Bi−0.3Cu−1In sample has the largest radius of capacitance arc, indicating that the sample has the best corrosion resistance. Figure 3(b) shows the

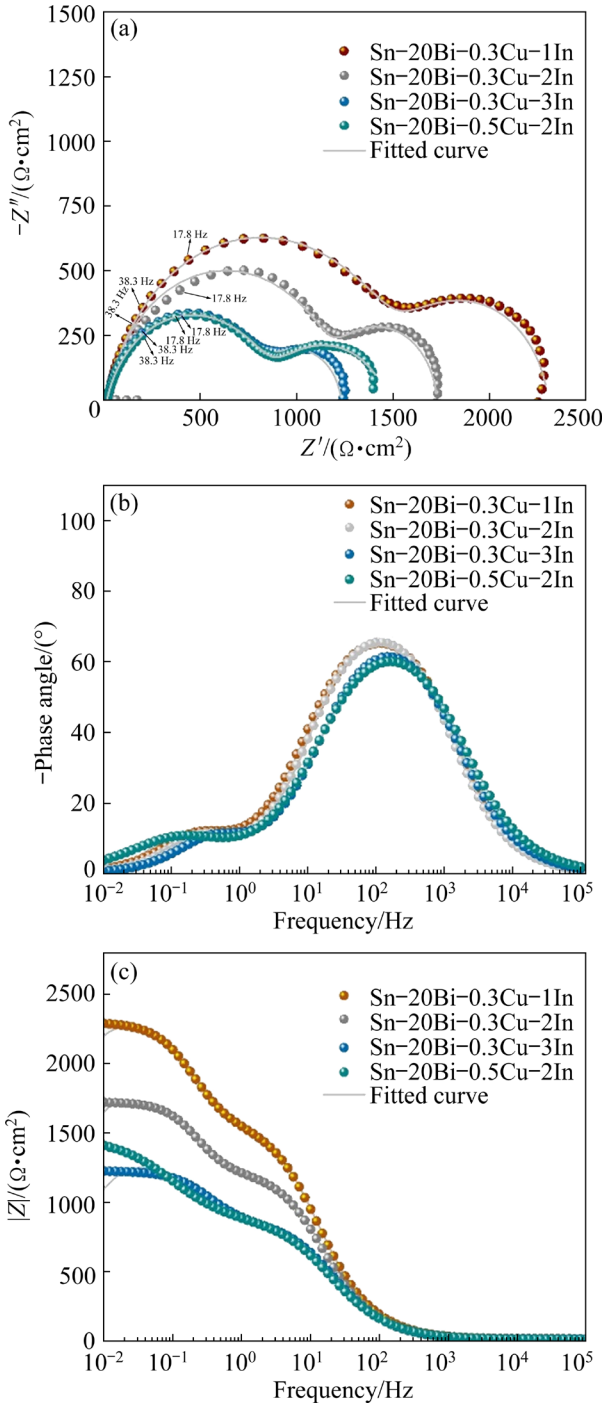

Fig. 3 EIS plots of Sn−20Bi−*x*Cu−*y*In alloy in 3.5 wt.% NaCl solution: (a) Nyquist plots; (b) Bode plots of phase angle vs frequency; (c) Bode plots of modulus vs frequency

phase angle versus frequency functions. There are two-time constants in the figure. According to CRUZ et al [21], phase angle values are above −45° when scanning from high to low frequency. The current is evenly distributed over the electrode surface in the lower frequency region. Larger value of the phase angle represents better combined corrosion resistance [22]. In Fig. 3(b), the presence of phase angle values higher than −45° for the four samples indicates a uniformly distributed electrode surface. The decreasing order of corrosion resistance is Sn−20Bi−0.3Cu−1In > Sn−20Bi−0.3Cu−2In > Sn−20Bi−0.5Cu−2In > Sn−20Bi−0.3Cu−3In.

Bode impedance plots are shown in Fig. 3(c). The high-frequency impedance value $|Z|$ corresponds to the corrosion product layer resistance R_{ct}. The low-frequency impedance value $|Z|$ represents the resistance (R_1) at the double-electric layer between the corrosion product layer and the solder substrate. $|Z|$ mainly manifests as the anodic dissolution process of the substrate, which is primarily affected by the protective ability of the corrosion product layer [19]. A higher value of $|Z|$ represents better corrosion resistance of the alloy [23], as shown in Fig. 3(c). The strength of the corrosion resistance is consistent with the above results. The analysis results of the three electrochemical impedance profiles are consistent. The order of corrosion resistance from strong to weak is as follows: Sn−20Bi−0.3Cu−1In > Sn−20Bi−0.3Cu−2In > Sn−20Bi−0.5Cu−2In > Sn−20Bi−0.3Cu−3In. Table 1 shows the impedance spectrum data.

From the data in Table 1, it is shown that the variations in R_{ct} and R_1 can reflect the formation process of the corrosion product layer and the corrosion rate of the substrate solder [17]. CPE_1 and CPE_{dl} are the capacitances associated with the pores on the surface of the composite and the double-electric layer, respectively. The fitting quality between experimental and simulated data is determined when Chi-squared values (χ^2) are analyzed [24]. The obtained impedance parameters, χ^2 and error ranges, are shown in Table 1. The sum of squares (provided by the CVIEW2 software) for each sample examined are also shown in Table 1.

The corrosion resistance of the alloy decreases with increasing In content. From Table 1, the R_{ct} values are 1566, 1216, and 860.5 Ω·cm^2, and the R_1 values are 717.4, 490.3, and 352.3 Ω·cm^2 when the Cu content is the same, and the In content is added at 1, 2, and 3 wt.%, respectively. Figure 4 provides a more intuitive representation of Table 1. The decrease in the R_{ct} value indicates that the increase in the In content reduces the resistance of corrosion product layer formation and promotes the formation of corrosion products. A decrease in the R_1 value

Table 1 Equivalent circuit parameters obtained by fitting EIS results of Sn−20Bi−*x*Cu−*y*In alloy in 3.5 wt.% NaCl solution

Parameter	Sn−20Bi−0.3Cu−1In	Sn−20Bi−0.3Cu−2In	Sn−20Bi−0.3Cu−3In	Sn−20Bi−0.5Cu−2In
R_s/(Ω·cm^2)	19.19±0.05	18.01±0.05	16.46±0.07	14.80±0.02
R_1/(Ω·cm^2)	717.4±15.04	490.3±10.97	352.3±12.59	590.0±8.07
R_{ct}/(Ω·cm^2)	1566.0±8.24	1216.0±6.27	860.5±7.78	866.5±2.78
R_t/(Ω·cm^2)	2283.4	1706.3	1212.8	1456.5
CPE$_1$/(μF·cm^2)	1217±37	1543±52	1504±83	2686±43
n_1	0.91	0.96	0.91	0.73
CPE$_{dl}$/(μF·cm^2)	20.6±0.19	21.4±0.23	25.6±0.47	30.1±0.18
n_{dl}	0.86	0.87	0.85	0.82
Sum of squares	0.11	0.14	0.3	0.03
χ^2	6.70×10^{-4}	9.10×10^{-4}	8.10×10^{-4}	1.80×10^{-4}

R_t is the sum of R_1 and R_{ct}, n is the CPE exponent, and CPE is equivalent to the pure resistance R for n=0 and pure capacitance for n=1

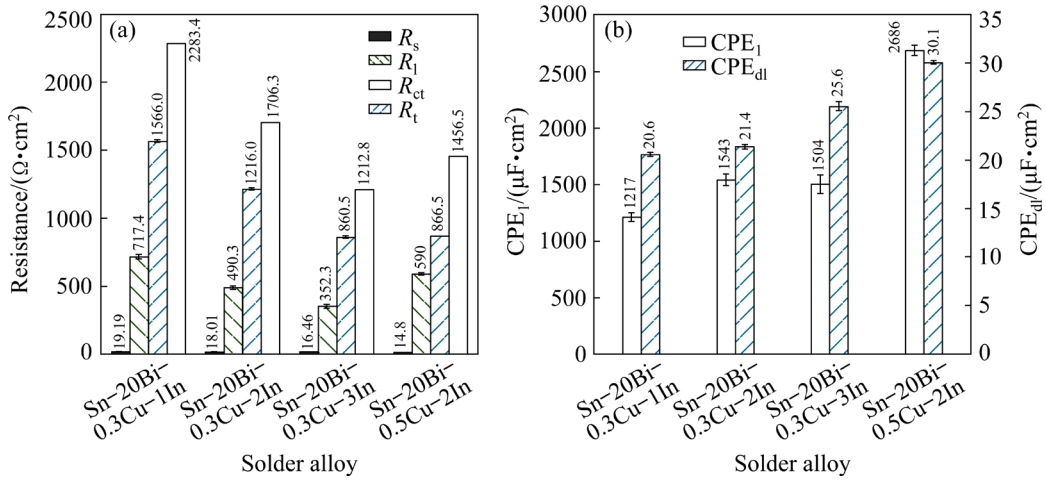

Fig. 4 Electrochemical impedance data of Sn−20Bi−*x*Cu−*y*In solder alloy: (a) R_s, R_1, R_{ct} and R_t; (b) CPE$_1$ and CPE$_{dl}$

indicates an increase in the anodic dissolution rate on the solder substrate [17]. Because the increase in the In content maintains the active state of the metal substrate (Sn), it increases the anodic dissolution rate and again promotes the corrosion reaction [25]. The values of R_{ct} are 1216.0 and 866.5 Ω·cm^2 when the In content is constant at 2 wt.%, and the Cu content is 0.3 and 0.5 wt.%, respectively. The former has a high resistance to the formation of the corrosion product layer. The R_1 values are 490.3 and 590.0 Ω·cm^2, respectively. The anodic dissolution rate of the former is faster than that of the latter. Cu usually reduces the corrosion resistance of alloys [26]. Therefore, when the Cu content increases to 0.5 wt.%, the R_{ct} value is lower than that of Sn−20Bi−0.3Cu−2In. This indicates a reduced resistance to corrosion product formation. The increase in trace Cu content reduces the corrosion resistance of the Sn−20Bi−*x*Cu−*y*In alloy. The scarcity of surface corrosion products does not cover the substrate solder surface well, increasing the contact area between the solder substrate and the corrosion solution, which increases the anodic dissolution rate. Thus, the R_1 value is relatively low [17].

HEAKAL et al [27] and LIU et al [28] reported that the total impedance value R_t, R_t=R_1+R_{ct}, could be used to qualitatively evaluate the corrosion resistance of an alloy. The inverse of the total impedance value is usually used to project the corrosion rate [27,29,30].

Table 1 expresses the total resistance of the alloy measured in a 3.5 wt.% NaCl solution. Sn−20Bi−0.3Cu−1In presents the highest R_t value

of 2283.4 Ω·cm^2, and Sn−20Bi−0.3Cu−3In presents the smallest R_t value of 1212.8 Ω·cm^2. The Sn−20Bi−0.3Cu−1In alloy has the best corrosion resistance, and the corrosion resistance strengths of the four alloys are consistent with the impedance plot analysis.

3.3 Potentiodynamic polarization curves

The potentiodynamic polarization curves of the Sn−20Bi−*x*Cu−*y*In composite solder in 3.5 wt.% NaCl solution are shown in Fig. 5, and the electrochemical corrosion parameters in Table 2 were obtained according to the Tafel extrapolation principle of electrochemical corrosion. For the convenience of comparison, the polarization curve parameters of three typical solders are listed in the latter part of Table 2. The corrosion resistance of Sn−20Bi−0.3Cu−1In is significantly better than that of Sn−9Zn, and it is very close to that of Sn−3.5Ag−0.5Cu and Sn−37Pb. The cathodic part of the polarization curve shows three different stages. In the first stage, the redox reaction occurs mainly on the electrode surface: $O_2+2H_2O+4e\rightarrow 4OH^-$. This section of the redox reaction can be divided into three steps [31]: (1) dissolved oxygen diffusion to the electrode surface, (2) charge transfer between the oxygen at the electrode and the solution interface, and (3) OH^- gathering from the reaction towards the specimen electrode. The second stage is dominated by the maximum diffusion of oxygen [32]. The terminal diffusion current density (J_{lim}) is proportional to the electrolyte thickness. According to the Nernst−Fick equation, the steady-state diffusion current density can be calculated in theory as follows:

$$J_{lim}=\frac{nFD_{O_2}}{\sigma}[O_2] \quad (1)$$

where n is the number of electrons required to reduce oxygen molecules, F is the Faraday constant, D_{O_2} is the diffusion coefficient of oxygen atoms, $[O_2]$ is the effective concentration of dissolved oxygen in the electrolyte layer, and σ is the thickness of the electrolyte. From Eq. (1), J_{lim} increases with the decreasing thickness of the electrolyte layer. In the third stage, because of the high cathodic potential, the primary reaction is the reduction of water [33].

Table 2 records the corrosion current density (J_{corr}), corrosion potential (φ_{corr}), corrosion rate, and polarization resistance (R_p) obtained from the Tafel extrapolation method. The R_p was calculated using CVIEW2 software based on the Stern−Geary equation as follows:

$$R_p=\frac{b_a b_c/[2.303(b_a+b_c)]}{J_{corr}} \quad (2)$$

R_p is the slope of the tangent line of the polarization curve at the corrosion potential. This is equivalent to the resistance value when the area of the corroded metal electrode is a unit value. b_a and b_c are the Tafel slopes of the common logarithms of the anode and cathode reactions, respectively.

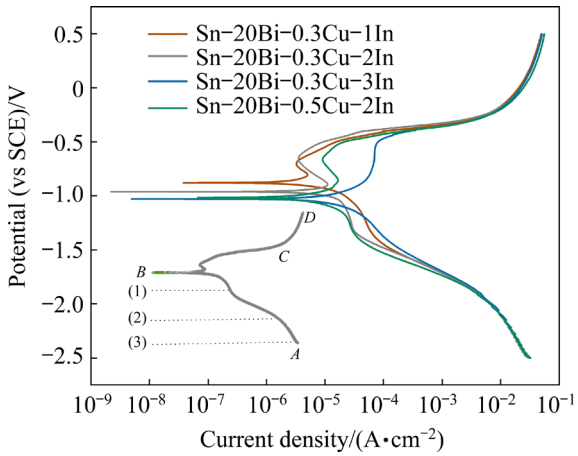

Fig. 5 Potentiodynamic polarization curves of Sn−20Bi−*x*Cu−*y*In composite solder

Table 2 Electrochemical parameters of Sn−20Bi−*x*Cu−*y*In alloy in 3.5 wt.% NaCl solution

Solder alloy	J_{corr}/(μA·cm^{-2})	φ_{corr}(vs SCE)/V	Corrosion rate/(mm·a^{-1})	R_p/(Ω·cm^2)
Sn−20Bi−0.3Cu−1In	7.17±0.51	−0.88±0.02	0.18±0.01	8411±23
Sn−20Bi−0.3Cu−2In	22.99±1.45	−0.96±0.02	0.58±0.02	6253±47
Sn−20Bi−0.3Cu−3In	44.49±5.24	−1.03±0.07	1.12±0.04	2748±24
Sn−20Bi−0.5Cu−2In	26.64±3.78	−1.02±0.05	0.67±0.04	5653±39
Sn−9Zn [25]	26.91	−0.94	−	976
Sn−3.5Ag−0.5Cu [25]	0.54	−0.61	−	46400
Sn−37Pb [25]	1.91	−0.59	−	8140

From the corrosion potential point of view, we can obtain Sn−20Bi−0.3Cu−1In, which has the best corrosion resistance. The corrosion resistance strength is consistent with the corrosion potential and impedance plot analysis. The larger the absolute value of the corrosion potential is, the greater the corrosion tendency is. From the corrosion potential, corrosion resistance of the alloy changes from strong to weak, i.e., Sn−20Bi−0.3Cu−1In > Sn−20Bi−0.3Cu−2In > Sn−20Bi−0.5Cu−2In > Sn−20Bi−0.3Cu−3In. From a corrosion current density point of view, the corrosion resistance of the alloy decreases with increasing In content when the Cu content is 0.3 wt.%. When the In content is 2 wt.%, the corrosion resistance of the alloy decreases with increasing Cu content. A smaller corrosion current density indicates a slower corrosion rate. According to Table 2, Sn−20Bi−*x*Cu−*y*In (*x*=0.3, 0.5 wt.%; *y*=1, 2, 3 wt.%) have corrosion current densities on the order of 7.17, 22.99, 44.49, and 26.64 μA/cm^2. When the Cu content is 0.3 wt.%, the corrosion current density increases with increasing In content. The increase of In content maintains the active state of the metal matrix (Sn), increases the anodic dissolution rate, and promotes the occurrence of the corrosion reaction again [25]. The corrosion current density of Sn−20Bi−0.3Cu−2In is lower than that of Sn−20Bi−0.5Cu−2In, which may be attributed to the addition of trace amount of Cu, thus increasing the intermetallic compound content of the solder alloy. TSAO and CHEN [34] showed that the corrosion current density increases with increasing Cu content. The increase in corrosion current density may be due to the formation of galvanic couples between Cu and Sn, intermetallic compounds (Cu_6Sn_5), and Sn-rich phases. The presence of both Cu_6Sn_5 and Cu_3Sn increases the corrosion current density values. SONG and LEE [35] investigated the corrosion behavior of Sn4Ag0.5Cu. They believed that the presence of Ag_3Sn in the solder accelerated the corrosion of Sn because of the galvanic couple corrosion mechanism. This result suggests that the generation of intermetallic compounds reduces the corrosion resistance of the alloy in 3.5 wt.% NaCl solution [26].

Figure 5 shows the electrochemical polarization curves of the Sn−20Bi−*x*Cu−*y*In solder alloys in 3.5 wt.% NaCl solution. The four alloys show the same corrosion behavior. According to the polarization curve, the process of polarization behavior can be divided into three stages: *AB*, *BC*, and *CD*. The cathodic reaction occurs between *A* and *B*. Point *B* is the cathodic transformation point, and the reaction is the dissolution of oxygen and hydrogen precipitation. First, the oxygen in the corrosion solution is dissolved, which is the electron reduction reaction of water:

$$O_2+2H_2O+4e=4OH^- \quad (3)$$

As shown in Fig. 1, when the oxygen in the solution is consumed, the polarization progresses, the Pt chip of the auxiliary electrode produces many bubbles, and the reaction is a hydrogen precipitation reaction. The reaction is

$$2H_2O+2e=2OH^-+H_2 \quad (4)$$

The cathodic polarization reaction stage process does not cause corrosion of the alloy. The surface remains bright, and no generation of corrosion products is observed. Point *B* is the cathodic−anodic transition point, and the potential corresponding to this point is the self-corrosion potential (φ_{corr}). The range of Points *B* and *C* is the anode reaction. The typical active metal dissolution behavior occurs in this range with increasing current density. Because the corrosion potential of the Bi-rich phase is positive, it is preserved as a cathode in the electrochemical corrosion reaction. The Sn-rich phase has a relatively low corrosion potential. The Sn phase is the anode to be selectively dissolved in the electrochemical reaction. According to the activity order of Sn, Bi, Cu, and In, metal dissolution behavior occurs only in the Sn phase. The reaction process is as follows:

$$Sn-2e=Sn^{2+} \quad (5)$$

$$Sn^{2+}-2e=Sn^{4+} \quad (6)$$

$$Sn+2OH^-=Sn(OH)_2+2e \quad (7)$$

$Sn(OH)_2$ is easily dehydrated to form SnO:

$$Sn(OH)_2=SnO+H_2O \quad (8)$$

Subsequently, $Sn(OH)_4$ is formed and dehydrated to produce SnO_2:

$$Sn(OH)_2+2OH^-=Sn(OH)_4+2e \quad (9)$$

$$SnO+H_2O+2OH^-=Sn(OH)_4+2e \quad (10)$$

$$Sn(OH)_4=SnO_2+2H_2O \quad (11)$$

$Sn_3O(OH)_2Cl_2$ is then produced, and the

reaction is

$$3Sn+4OH^-+2Cl^-=Sn_3O(OH)_2Cl_2+H_2O \quad (12)$$

After that, pseudo passivation is observed when the potential reaches Point *C*. The *CD* segment is a pseudo passivation stage [36]. The current density is maintained at approximately 0.5 A/cm^2. Notably, pseudo passivation results from the physical protection of the thick corrosion products on the working surface instead of a passivation process. Further corrosion can be prevented because the products can prevent contact between the solder substrate and the etching solution.

3.4 Corrosion products

The corrosion product layer on the surface of the Sn−20Bi−*x*Cu−*y*In alloy sample was identified by XRD, EDS, and XPS analysis. As shown in Fig. 6(a), the XRD patters showed that the corrosion product in the solder in 3.5 wt.% NaCl solution was $Sn_3O(OH)_2Cl_2$. Combined with EDS analysis, the corrosion product was verified to be $Sn_3O(OH)_2Cl_2$ again. Figure 6(b) shows the XRD pattern of Sn−20Bi−0.3Cu−3In sample without the corrosion test. It can be observed from Fig. 6(b) that there are only peaks of Sn and Bi in the spectral line. A small amount of In is in the solid solution in the matrix. The content of added Cu is minimal, part of which is solid-solution in the matrix, and the other part generates trace amount of alloy compounds. Therefore, it could not be detected by XRD. As shown in Fig. 7. The corrosion products of Sn−20Bi−0.3Cu−1In are mainly composed of Sn, O, and Cl. The high-resolution spectra of Sn 3$d_{5/2}$, O 1s, and Cl 2p are shown in Fig. 8. The Sn 3$d_{5/2}$ spectrum has three fitted peaks, as shown in Fig. 8(a). Three Gaussian functions centered at 485.2, 485.9, and 486.2 eV represent Sn^0, Sn^{2+}, and Sn^{4+}, respectively. Figure 8(b) shows the O 1s spectrum. The peak at 530.2 eV can be attributed to the oxygen of the oxide, and the peak at 531.8 eV belongs to the carboxyl oxygen. Figure 8(c) is the Cl 2p spectrum, with two peaks at 197.7 and 200.0 eV.

This 200.0 eV peak corresponds to Sn^{2+} and Sn^{4+} chlorides and possibly chlorine oxides and hydroxyl chlorides. The value of 197.7 eV for Cl 2p could be a residual of sodium chloride.

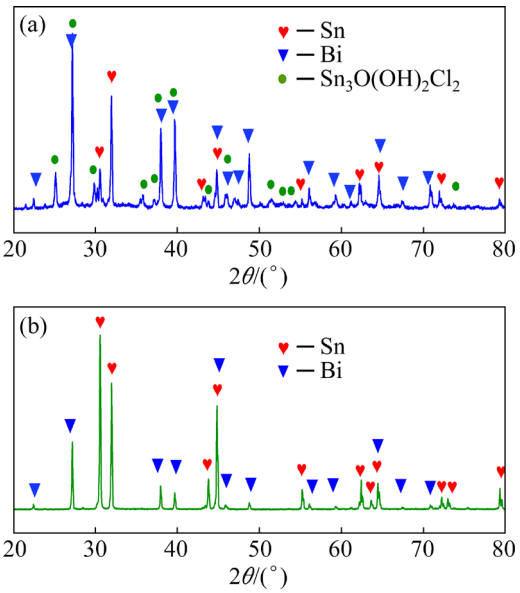

Fig. 6 XRD patterns of solder surface after Sn−20Bi−0.3Cu−3In polarization test: (a) After corrosion test; (b) Before corrosion test

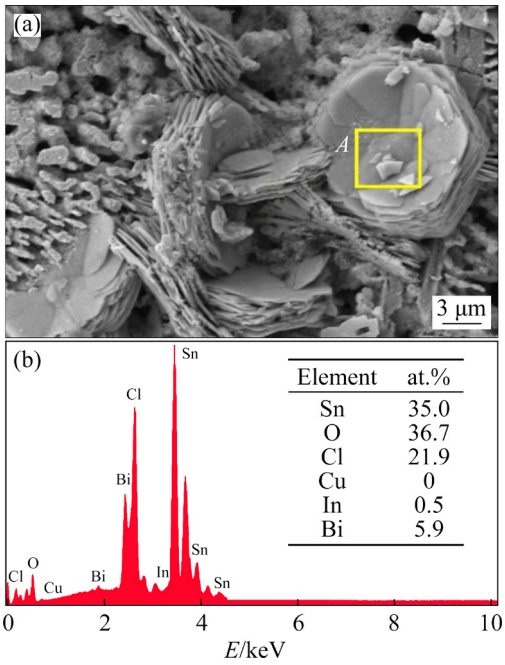

Fig. 7 EDS analysis results of Sn−20Bi−0.3Cu−1In solder: (a) SEM image; (b) EDS data at Point *A* in (a)

The formation of these compounds leads to an increase in the local volume of the solder [26]. The formation of disc-like compounds is shown in Fig. 9. Sn−20Bi−*x*Cu−*y*In solder alloy generates a mixture of disc-like corrosion products covering the surface of the solder after polarization tests in NaCl solution. Figure 9 shows the surface corrosion morphology of the solder after corrosion in a 3.5 wt.% NaCl solution. From the electrochemical

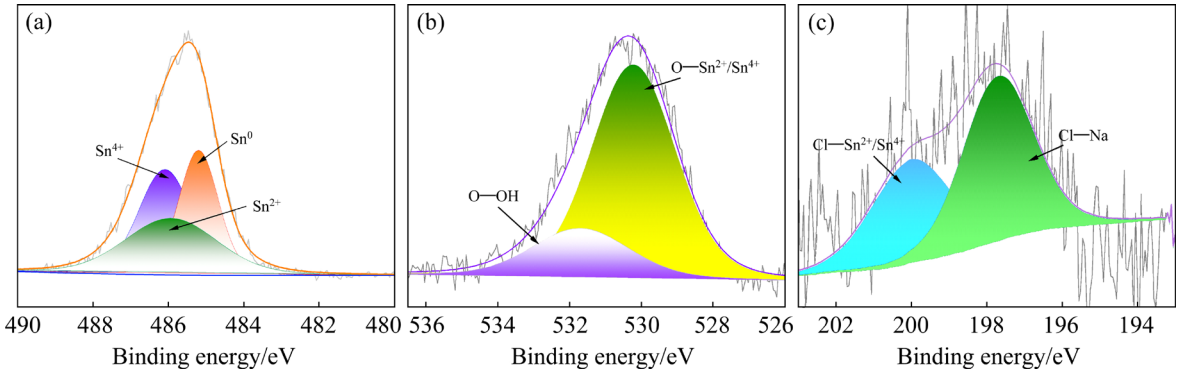

Fig. 8 XPS spectra of Sn−20Bi−0.3Cu−1In solder alloy measured in 3.5 wt.% NaCl solution: (a) Sn $3d_{5/2}$; (b) O 1s; (c) Cl 2p

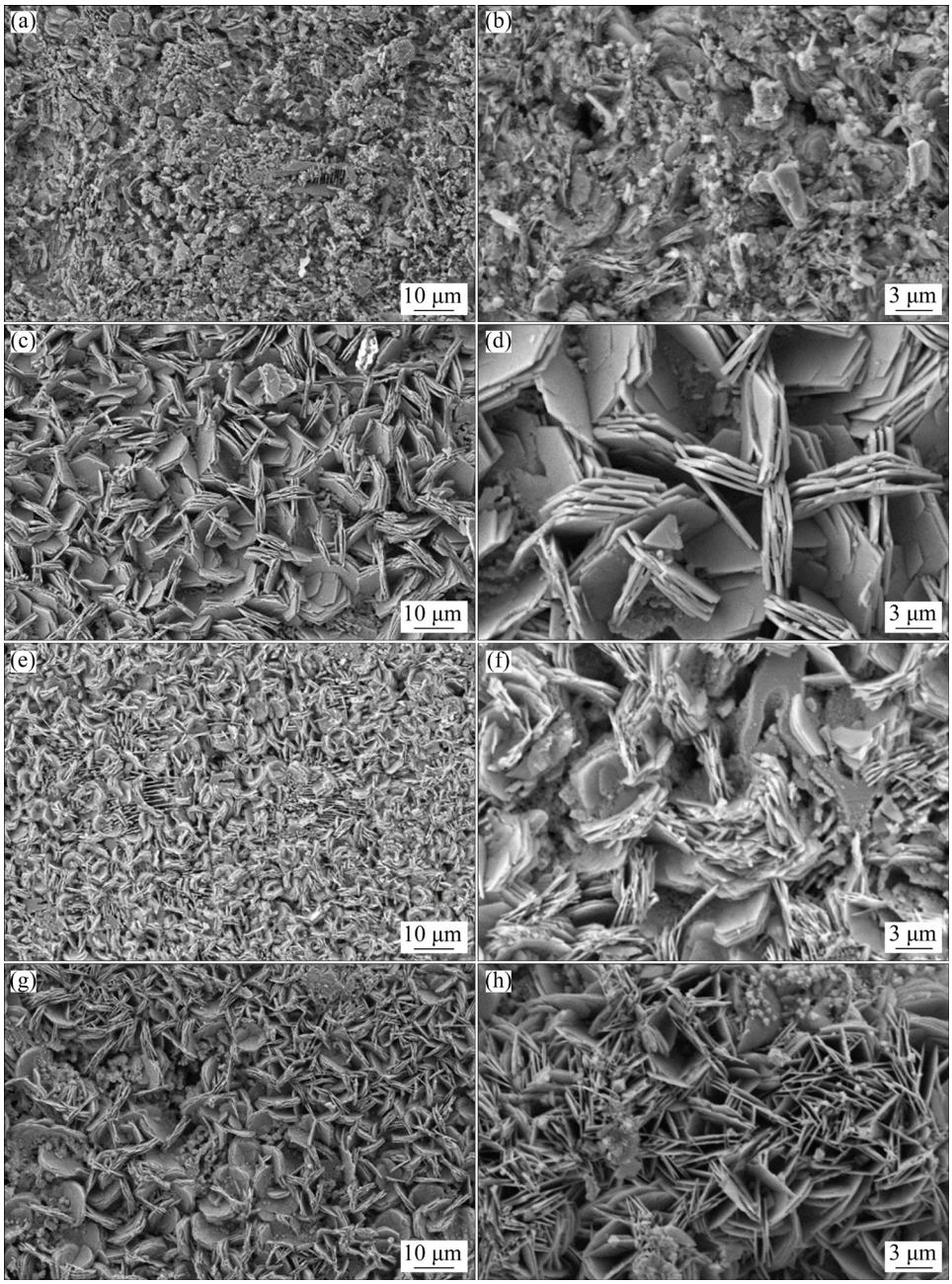

Fig. 9 Surface corrosion morphologies of Sn−20Bi−*x*Cu−*y*In (*x*=0.3, 0.5 wt.%; *y*=1, 2, 3 wt.%): (a, b) Sn−20Bi−0.3Cu−1In; (c, d) Sn−20Bi−0.3Cu−2In; (e, f) Sn−20Bi−0.3Cu−3In; (g, h) Sn−20Bi−0.5Cu−2In

corrosion morphology, the microstructure of corrosion products on different solders is similar and densely dispersed on the surface of the solder. As shown in Fig. 10, the increase in corrosion products on the surface of the solder leads to an increase in the local volume of the solder. Corrosion products appear to be stacked on top of each other and squeezed. The yellow rectangle in Fig. 10 shows holes between the corrosion products. The enlarged area of the disc-like corrosion product shows gaps between the layers, and the adhesion is poor. Because these features of the corrosion product layer cannot stop the electrolyte from getting through, the electrolyte can keep contacting with the matrix through holes and other flaws, which causes the corrosion reaction to continue.

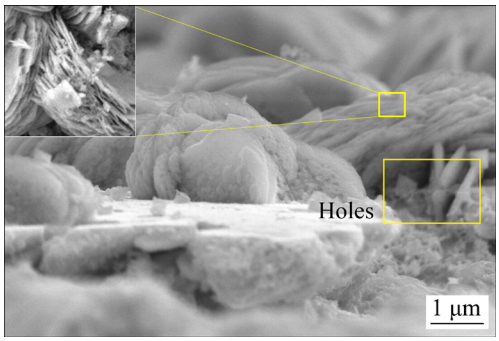

Fig. 10 Corrosion morphology of cross-section of Sn−20Bi−0.3Cu−3In solder alloy

Therefore, the galvanic effect induced by the microstructure will still come into playing and last for a long time when the surface corrosion product layer is non-adherent and cracks. However, this primary cell effect decreases when the surface corrosion product layer is dense and adheres to the solder substrate. Then, the protective effect of the corrosion product layer will become dominant [37].

As shown in Fig. 11, a comprehensive explanation is given for the decrease in the corrosion resistance of the Sn−20Bi−*x*Cu−*y*In alloy with increasing In content. WU et al [25] found that adding In to Sn−3.5Ag−0.5Cu solder reduced the corrosion resistance in a 3.5 wt.% NaCl solution. The microstructural change caused by alloying is the main reason for the decrease in corrosion resistance. The strong interaction of In with OH^- and Cl^- leads to the increased anodic dissolution. This also indicates that the presence of In ensures the accumulation of adsorbed Cl^- on the sample surface and maintains the active state of the metal matrix Sn [38]. With an increase in the In content from 1 to 3 wt.% in the Sn−20Bi−0.3Cu−*y*In alloy, more Cl^- and OH^- in solution are adsorbed on the solder surface. The anodic dissolution rate increases and promotes further corrosion reactions.

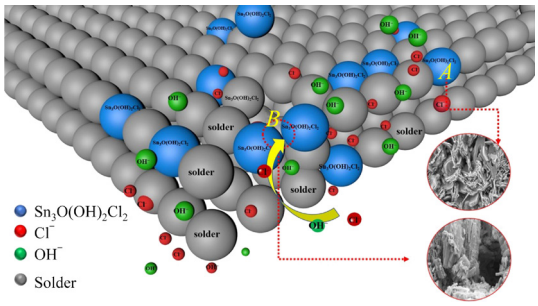

Fig. 11 Schematic diagram showing corrosion mechanism of Sn−20Bi−*x*Cu−*y*In (*x*=0.3, 0.5 wt.%; *y*=1, 2, 3 wt.%)

Because the increase in the In content maintains the active state of the metal matrix (Sn), more Sn is involved in the reaction. At the same time, In can absorb more Cl^- and OH^- ions. Therefore, Reaction (12) is promoted, and the formation of corrosion products is further promoted. Blue spheres represent corrosion products, gray spheres represent solder alloys, and red and green spheres represent Cl^- and OH^- ions, as shown in Fig. 11. Area *A* in the figure represents the top view of the corrosion product. Combined with Fig. 9, it can be observed that the corrosion product is disc-like, and there are gaps between the layers. Region *B* represents the gap between corrosion products, and there are significant gaps between corrosion products. These gaps allow Cl^- and OH^- ions to further react with the solder substrate. The corrosion resistance of the alloy decreases with increasing In content.

4 Conclusions

(1) Based on the capacitive semi-arcs, phase angle, impedance modulus $|Z|$, R_1, R_{ct}, and potentiodynamic polarization curves, the corrosion resistance of Sn−20Bi−*x*Cu−*y*In (*x*=0.3, 0.5 wt.%; *y*=1, 2, 3 wt.%) solder in 3.5 wt.% NaCl solution decreases with increasing In content.

(2) The corrosion resistance of the alloy decreases slightly with the increase of Cu content.

(3) According to XRD phase identification, XPS, and EDS analysis, it was determined that the

corrosion product on the surface of the Sn−20Bi−*x*Cu−*y*In alloy sample was $Sn_3O(OH)_2Cl_2$.

(4) By comprehensive analysis of Sn−20Bi−*x*Cu−*y*In (*x*=0.3, 0.5 wt.%; *y*=1, 2, 3 wt.%), the order of corrosion resistance from strong to weak is Sn−20Bi−0.3Cu−1In > Sn−20Bi−0.3Cu−2In > Sn−20Bi−0.5Cu−2In > Sn−20Bi−0.3Cu−3In.

Acknowledgments

This work was supported by the Guangxi Natural Science Foundation, China (Nos. 2020GXNSFBA297062, 2018GXNSFDA050008, 2020GXNSFAA159093), the National Natural Science Foundation of China (No. 51761002), and the Training Plan of High-level Talents of Guangxi University, China (No. XMPZ160714).

References

[1] WU Ming, WANG Shan-lin, SUN Wen-jun, HONG Min, CHEN Yu-hua, KE Li-ming. Fracture pattern evolution of SnAgCu−SnPb mixed solder joints at cryogenic temperature [J]. Transactions of Nonferrous Metals Society of China, 2021, 31(9): 2762−2772.

[2] DONG Ming-jie, GAO Zhi-ming, LIU Yong-chang, WANG Xun, YU Li-ming. Effect of indium addition on the microstructural formation and soldered interfaces of Sn−2.5Bi−1Zn−0.3Ag lead-free solder [J]. International Journal of Minerals, Metallurgy, and Materials, 2012, 19(11): 1029−1035.

[3] JAFFERY H A, SABRI M F M, SAID S M, HASAN S W, SAJID I H, NORDIN N I M, MEGAT HASNAN M M I, SHNAWAH D A, MOORTHY C V. Electrochemical corrosion behavior of Sn−0.7Cu solder alloy with the addition of bismuth and iron [J]. Journal of Alloys and Compounds, 2019, 810: 151925.

[4] CHENG S C, LIN K L. The thermal property of lead-free Sn−8.55Zn−1Ag−*X*Al solder alloys and their wetting interaction with Cu [J]. Journal of Electronic Materials, 2002, 31(9): 940−945.

[5] KIM B, LEE C W, LEE D Y, KANG N. Effect of Sb addition on Bi−2.6Ag−0.1Cu solders for high-temperature applications [J]. Journal of Alloys and Compounds, 2014, 592: 207−212.

[6] NORDIN N I M, SAID S M, RAMLI R, SABRI M F M, SHARIF N M, ARIFIN N A F N M, IBRAHIM N N S. Microstructure of Sn−1Ag−0.5Cu solder alloy bearing Fe under salt spray test [J]. Microelectronics Reliability, 2014, 54: 2044−2047.

[7] AMAGAI M, TOYODA Y, OHNISHI T, AKITA S. High drop test reliability: Lead-free solders [C]//Proceedings of the 54th Electronic Components and Technology Conference. Las Vegas, NV, USA, LEEE, 2004: 1304−1309.

[8] CHANTARAMANEE S, SUNGKHAPHAITOON P. Influence of bismuth on microstructure, thermal properties, mechanical performance, and interfacial behavior of SAC305−*x*Bi/Cu solder joints [J]. Transactions of Nonferrous Metals Society of China, 2021, 31(5): 1397−1410.

[9] TUNTHAWIROON P, KANLAYASIRI K. Effects of Ag contents in Sn−*x*Ag lead-free solders on microstructure, corrosion behavior and interfacial reaction with Cu substrate [J]. Transactions of Nonferrous Metals Society of China, 2019, 29(8): 1696−1704.

[10] ZHANG Cheng, LIU Si-dong, QIAN Guo-tong, ZHOU Jian, XUE Feng. Effect of Sb content on properties of Sn−Bi solders [J]. Transactions of Nonferrous Metals Society of China, 2014, 24(1): 184−191.

[11] ROSALBINO F, ANGELINI E, ZANICCHI G, MARAZZA R. Corrosion behaviour assessment of lead-free Sn−Ag−M (M=In, Bi, Cu) solder alloys [J]. Materials Chemistry and Physics, 2008, 109(2): 386−391.

[12] LI De-zhi, CONWAY P P, LIU Chang-qing. Corrosion characterization of tin−lead and lead free solders in 3.5 wt.% NaCl solution [J]. Corrosion Science, 2008, 50(4): 995−1004.

[13] LIN K L, LIU T P. The electrochemical corrosion behaviour of Pb-free Al−Zn−Sn solders in NaCl solution [J]. Materials Chemistry and Physics, 1998, 56(2): 171−176.

[14] QUARTARONE G, BELLOMI T, ZINGALES A. Inhibition of copper corrosion by isatin in aerated 0.5 M H_2SO_4 [J]. Corrosion Science, 2003, 45(4): 715−733.

[15] ZHANG Xue-lin, JIANG Zhao-hua, YAO Zhong-ping, SONG Ying, WU Zheng-de. Effects of scan rate on the potentiodynamic polarization curve obtained to determine the Tafel slopes and corrosion current density [J]. Corrosion Science, 2009, 51(3): 581−587.

[16] BRUG G J, EEDEN V D, REHBACH M S, SLUYTERS J H. The analysis of electrode impedances complicated by the presence of a constant phase element [J]. Journal of Electroanalytical Chemistry and Interfacial Electrochemistry, 1984, 176(1): 275−295.

[17] QIAO Chuang, WANG Ming-na, HAO Long, JIANG Xiao-lin, LIU Xia-he, THEE C, AN Xi-zhong. In-situ EIS study on the initial corrosion evolution behavior of SAC305 solder alloy covered with NaCl solution [J]. Journal of Alloys and Compounds, 2021, 852: 156953.

[18] SATIZABAL L M, COSTA D, MORAES P B, BORTOLOZO A D, OSÓRIO W R. Microstructural array and solute content affecting electrochemical behavior of Sn−Ag and Sn−Bi alloys compared with a traditional Sn−Pb alloy [J]. Materials Chemistry and Physics, 2019, 223: 410−425.

[19] LIU Jian-chun, ZHANG Gong, MA Ju-sheng, SUGANUMA K. Ti addition to enhance corrosion resistance of Sn−Zn solder alloy by tailoring microstructure [J]. Journal of Alloys and Compounds, 2015, 644: 113−118.

[20] YUAN Shao-jun, CHOONG A M F, PEHKONEN S O. The influence of the marine aerobic *Pseudomonas* strain on the corrosion of 70/30 Cu−Ni alloy [J]. Corrosion Science, 2007, 49(12): 4352−4385.

[21] CRUZ R P V, NISHIKATA A, TSURU T. Pitting corrosion mechanism of stainless steels under wet-dry exposure in chloride-containing environments [J]. Corrosion Science, 1998, 40(1): 125−139.

[22] GAO Yan-fang, CHENG Cong-qian, ZHAO Jie, WANG Li-hua, LI Xiao-gang. Electrochemical corrosion of Sn−0.75Cu solder joints in NaCl solution [J]. Transactions of Nonferrous Metals Society of China, 2012, 22(4): 977−982.
[23] LIU Jian-chun, WANG Zheng-hong, XIE Jing-yang, MA Ju-sheng, ZHANG Gong, SUGANUMA K. Effects of intermetallic-forming element additions on microstructure and corrosion behavior of Sn−Zn solder alloys [J]. Corrosion Science, 2016, 112: 150−159.
[24] MEYER Y A, BONATTI R S, BORTOLOZO A D, OSÓRIO W R. Electrochemical behavior and compressive strength of Al−Cu/*x*Cu composites in NaCl solution [J]. Journal of Solid State Electrochemistry, 2021, 25(4): 1303−1317.
[25] WU Bai-yan, CHAN Yan-cheong, ALAM M O, JILLEK W. Electrochemical corrosion study of Pb-free solders [J]. Journal of Materials Research, 2006, 21(1): 62−70.
[26] OSÓRIO W R, FREIRE C M, CARAM R, GARCIA A. The role of Cu-based intermetallics on the pitting corrosion behavior of Sn−Cu, Ti−Cu and Al−Cu alloys [J]. Electrochimica Acta, 2012, 77: 189−197.
[27] HEAKAL F E T, FEKRY A M, GHONEIM A A. Corrosion characterization of new tin−silver binary alloys in nitric acid solutions [J]. Corrosion Science, 2008, 50(6): 1618−1626.
[28] LIU Jian-chun, ZHANG Gong, WANG Zheng-hong, XIE Jing-yang, MA Ju-sheng, SUGANUMA K. Electrochemical behavior of Sn−*x*Zn lead-free solders in aerated NaCl solution [C]//Proceedings of the 16th International Conference on Electronic Packaging Technology. Changsha, China, 2015: 68−83.
[29] LIU Jian-chun, PARK S W, NAGAO S, NOGI M, KOGA H, MA Ju-sheng, ZHANG Gong, SUGANUMA K. The role of Zn precipitates and Cl^- anions in pitting corrosion of Sn−Zn solder alloys [J]. Corrosion Science, 2015, 92: 263−271.
[30] YIN Mo-yang, LI Zhou, XIAO Zhu, PANG Yong, LI Ya-ping, SHEN Zi-yan. Corrosion behavior of Cu−Al−Mn−Zn−Zr shape memory alloy in NaCl solution [J]. Transactions of Nonferrous Metals Society of China, 2021, 31(4): 1012−1022.
[31] NISHIKATA A, ICHIHARA Y, HAYASHI Y, TSURU T. Influence of electrolyte layer thickness and pH on the initial stage of the atmospheric corrosion of iron [J]. Journal of the Electrochemical Society, 1997, 144(4): 1244−1252.
[32] ZHOU He-rong, LI Xiao-gang, MA Jian, DONG Chao-fang, HUANG Yi-zhong. Dependence of the corrosion behavior of aluminum alloy 7075 on the thin electrolyte layers [J]. Materials Science and Engineering B, 2009, 162(1): 1−8.
[33] ZHONG Xian-kang, ZHANG Guo-an, QIU Yu-bin, CHEN Zhen-yu, GUO Xing-peng, FU Chao-yang. The corrosion of tin under thin electrolyte layers containing chloride [J]. Corrosion Science, 2013, 66: 14−25.
[34] TSAO L C, CHEN C W. Corrosion characterization of Cu−Sn intermetallics in 3.5 wt.% NaCl solution [J]. Corrosion Science, 2012, 63: 393−398.
[35] SONG F B, LEE S W R. Corrosion of Sn−Ag−Cu lead-free solders and the corresponding effects on board level solder joint reliability [C]//Proceedings of the 56th Electronic Components and Technology Conference. Hong Kong: IEEE, 2006: 891−898.
[36] WANG Zheng-hong, CHEN Chuan-tong, JIU Jin-ting, NAGAO S, NOGI M, KOGA H, ZHANG Hao, ZHANG Gong, SUGANUMA K. Electrochemical behavior of Zn−*x*Sn high-temperature solder alloys in 0.5 M NaCl solution [J]. Journal of Alloys and Compounds, 2017, 716: 231−239.
[37] WANG Ming-na, QIAO Chuang, JIANG Xiao-lin, HAO Long, LIU Xia-he. Microstructure induced galvanic corrosion evolution of SAC305 solder alloys in simulated marine atmosphere [J]. Journal of Materials Science & Technology, 2020, 51: 40−53.
[38] MUÑOZ A G, SAIDMAN S B, BESSONE J B. Influence of In on the corrosion of Zn−In alloys [J]. Corrosion Science, 2001, 43(7): 1245−1265.

Sn−20Bi−*x*Cu−*y*In 焊料在 3.5% NaCl 溶液中的腐蚀特性

祁 达[1,2,3]，杨文超[1,2,3]，蒋仕伟[1,2,3]，傅耀坤[1,2,3]，宋浅浅[1,2,3]，湛永钟[1,2,3]

1. 广西大学 资源环境与材料学院，南宁 530004；
2. 省部共建特色金属与组合结构全寿命安全国家重点实验室，南宁 530004；
3. 有色金属及材料加工新技术教育部重点实验室，南宁 530004

摘 要：研究室温条件下 Sn−20Bi−*x*Cu−*y*In (*x*=0.3%，0.5%，质量分数；*y*=1%，2%，3%，质量分数)合金在 3.5%(质量分数)NaCl 溶液中的腐蚀行为。采用电化学阻抗谱图(EIS)、动电位极化曲线和表面腐蚀产物表征研究焊料的耐腐蚀性能。EIS 和极化曲线结果表明，随着 In 和 Cu 含量的增加，焊料的耐腐蚀性能降低。采用扫描电镜、能量色散光谱、X 射线衍射和 X 射线光电子能谱对腐蚀产物进行表征。腐蚀产物 $Sn_3O(OH)_2Cl_2$ 结构松散，不能起到保护作用。Sn−20Bi−0.3Cu−1In 的耐腐蚀性能最好。

关键词：无铅焊料；腐蚀行为；电化学阻抗谱；极化曲线；$Sn_3O(OH)_2Cl_2$

(Edited by Wei-ping CHEN)